Matrix-Valued Radial Basis Functions for Local Vector Field Reconstruction in Computational Fluid Dynamic Models

J. Baudisch*, L. Bonaventura♯, A. Iske♯♯, E. Miglio♯

10th January 2006

* Department of Mathematics, Munich University of Technology,
D-85747 Garching, Germany
jan.baudisch@gmx.net

♯ MOX– Modellistica e Calcolo Scientifico
Dipartimento di Matematica "F. Brioschi"
Politecnico di Milano
via Bonardi 9, 20133 Milano, Italy
luca.bonaventura@polimi.it,edie.miglio@mate.polimi.it

♯♯ Department of Mathematics, University of Hamburg,
D-20146 Hamburg, Germany
iske@math.uni-hamburg.de

Keywords: Radial Basis Functions, vector field reconstruction, Raviart-Thomas (RT) elements, computational fluid dynamics

AMS Subject Classification: 41A05, 41A63, 65D05, 65M60, 86A05, 86A10

Abstract

Matrix-valued radial basis functions (RBFs) are applied to obtain accurate local vector field reconstructions from normal components assigned at the edges of a computational mesh. The theory of RBF reconstruction for vector-valued functions is first reviewed, before it is adapted to specific requirements from relevant applications in computational fluid dynamics. Important computational aspects of the utilized RBF reconstruction, such as stencil selection, are explained in detail, which makes the method more accessible to similar problems in geophysical fluid dynamics and related applications. Extensive numerical comparisons concerning models from hydrodynamic problems show that the proposed RBF reconstruction method significantly improves the accuracy of standard discretizations, while retaining discrete conservation properties of important physical quantities, such as mass, vorticity or potential enstrophy.

1 Introduction

Radial basis functions (RBFs) are powerful tools for interpolation and approximation of scalar-valued multivariate functions from scattered data, see [1, 2, 3] for a recent account on theorectical and practical aspects of RBFs and their applications. RBFs are well-known to provide highly accurate reconstructions, without imposing too severe restrictions on the spatial distribution of the sample points where the data are assumed to be known.

In fact, spectral convergence rates can be achieved for RBF interpolation methods, when appropriate types of radial basis functions, such as Gaussians or (inverse) multiquadrics, are chosen. Moreover, it can be shown that in this case also any derivative of the interpolated function can be approximated just as accurately by the corresponding derivative of the RBF interpolator, see [3, Chapter 11].

Quite recently, many different meshfree methods were developed to numerically solve partial differential equations by using RBF techniques, where the utilized approaches include collocation methods [4, 5], Galerkin methods [6], and semi-Langrangian discretizations [7, 8], to mention but a few.

But the utility of RBF methods has also been shown for mesh-based methods, such as for instance in [9, 10] where radial basis functions were used to obtain highly accurate finite volume ENO schemes by local RBF reconstruction from scattered cell average values. Another example is the recent adaptive ADER scheme [11], where RBF interpolation is used to construct appropriate error estimators for mesh adaption, i.e., coarsening and refinement of triangular mesh cells. Moreover, RBFs were used in [12] to develop high order approximation schemes for discretizing differential operators of the shallow water equations. Similar interpolation approaches based on kriging have also been applied in [13]. In [14, 15], RBF interpolation is essential to achieve accurate semi-Lagrangian schemes on Cartesian grids with cut boundary cells. In all these applications,

scalar-valued RBFs were used for local interpolation, which allows one to reconstruct a function at any point in space, given its *scalar* values in a neighbourhood of that point.

In this paper, we aim at pursuing further this development by using *matrix-valued* RBFs for the interpolation of *vector-valued* functions. The general setting of Hermite-Birkhoff interpolation via matrix-valued RBFs is covered in the seminal paper [16] of Narcowich and Ward, where in particular the well-posedness of the reconstruction problem is explained. Although we believe that the 1994 paper [16] has remarkably great potential for applications in computational fluid dynamics and related fields, it seems that the rather technical work [16] has not gained much attention in applications since then.

In the present paper, relevant theoretical details from [16] are first reviewed, before some of the theory is adapted to the particular requirements from those applications in computational fluid dynamics which we wish to address here. In this way, we also wish to make the results of [16] more accessible. The primary goal of this paper, however, is to provide accurate vector field approximations by RBF reconstruction in order to improve standard finite element discretizations, such as low order Raviart-Thomas (RT) elements, see [17, 18].

In such RT finite element methods, discrete vector fields are usually represented by their components normal to the edges of the computational mesh. Relevant applications of RT elements include electromagnetic [19] and hydrodynamical problems, the latter being the focus of the present paper. Although higher order RT elements were developed, low order ones lead more easily to numerical methods that exhibit appealing mimetic properties, such as conservation of mass, vorticity and potential enstrophy. But recent methods from applications in hydrodynamics, such as [20, 21, 22, 23], rely on the above mentioned conservation properties. The RBF reconstruction method which we propose in this paper allows us to enhance the accuracy of low order RT elements, while retaining their important discrete conservation properties.

The outline of this paper is as follows. In Section 2, key features of vector field reconstruction by RBF interpolation are first reviewed, before the specific vector reconstruction problem is explained in Section 3. Important practical aspects concerning the implementation of the proposed RBF reconstruction method are addressed, including the construction of customized stencils. In Section 4, the accuracy of the resulting RBF reconstruction scheme is assessed in comparison with RT elements of order zero, RT_0. This is done on the basis of specific numerical tests, where accuracy rates are determined numerically for both methods, RBF reconstruction and the RT elements RT_0. Finally, in Section 5, the practical relevance of the proposed RBF vector field reconstruction is demonstrated by using two different shallow water models, aiming at atmospheric and coastal modelling, respectively.

2 Vector Field Reconstruction from Hermite-Birkhoff Data

This section addresses the reconstruction of vector-valued functions from scattered Hermite-Birkhoff data. In order to explain this problem, let $u : \mathbb{R}^d \to \mathbb{R}^n$ denote a vector-valued function, $u = (u_1, \ldots, u_n)$. Moreover, assume that for a finite set $\Lambda = \{\lambda\}_{\lambda \in \Lambda}$ of linearly independent vector-valued linear functionals, samples $\lambda(u) \in \mathbb{R}$ are given, where the action of any $\lambda = (\lambda_1, \ldots, \lambda_n) \in \Lambda$ on u is defined as

$$\lambda(u) = \sum_{k=1}^{n} \lambda_k(u_k).$$

Reconstruction of u from values $\{\lambda(u) : \lambda \in \Lambda\}$ requires finding a recovery function $s : \mathbb{R}^d \to \mathbb{R}^n$ satisfying

$$\lambda(s) = \lambda(u), \qquad \text{for all } \lambda \in \Lambda, \tag{1}$$

or, $s\big|_\Lambda = u\big|_\Lambda$, in short hand notation. The approach taken in this paper works with matrix-valued radial basis functions (RBFs), as suggested in the seminal paper [16] by Narcowich and Ward.

In order to explain reconstruction by matrix-valued RBFs, let $\mathbf{\Phi} : \mathbb{R}^d \to \mathbb{R}^{n \times n}$ be a matrix-valued function, with scalar-valued components $\phi_{jk} : \mathbb{R}^d \to \mathbb{R}$, i.e.,

$$\mathbf{\Phi}(\mathbf{x}) = (\phi_{jk}(\mathbf{x}))_{1 \le j,k \le n} \in \mathbb{R}^{n \times n}, \qquad \text{for } \mathbf{x} \in \mathbb{R}^d, \tag{2}$$

and, moreover, we assume that $\mathbf{\Phi}$ is even, i.e., $\mathbf{\Phi}(\mathbf{x}) = \mathbf{\Phi}(-\mathbf{x})$. For any functional λ, the convolution product $\lambda * \mathbf{\Phi} : \mathbb{R}^d \to \mathbb{R}^n$ is defined componentwise as

$$[\lambda * \mathbf{\Phi}]_j(\mathbf{x}) = \sum_{k=1}^{n} \lambda_k \phi_{jk}(\mathbf{x} - \cdot), \qquad \text{for } 1 \le j \le n.$$

Suitable entries for the components of $\mathbf{\Phi}$ in (2) are *radial* basis functions, $\phi(r) \equiv \phi_{jk}(r)$, $r = \|\mathbf{x}\|$, where popular choices include Gaussians, $\phi(r) = e^{-r^2}$, multiquadrics, $\phi(r) = \sqrt{1 + r^2}$, and inverse multiquadrics, $\phi(r) = 1/\sqrt{1 + r^2}$.

According to the RBF reconstruction scheme, the interpolant s in (1) is required to have the form

$$s = \tau * \mathbf{\Phi} + p, \tag{3}$$

where the dual functional τ is a linear combination of elements in Λ,

$$\tau = \sum_{\mu \in \Lambda} c_\mu \mu,$$

and where $p : \mathbb{R}^d \to \mathbb{R}^n$ is a vector-valued polynomial, $p = (p_1, \ldots, p_n)$, in d variables, each of whose components $p_j : \mathbb{R}^d \to \mathbb{R}$, $1 \le j \le n$, is, for some specific m depending on $\mathbf{\Phi}$, of order at most m. We collect all such polynomials in the linear space $\mathcal{P}_m^{d,n}$.

Note that the interpolant s in (3) contains a vector $c = (c_\mu)_{\mu\in\Lambda} \in \mathbb{R}^N$ of $N = |\Lambda|$ unknown coefficients in its major part $\tau * \mathbf{\Phi}$, and $Q = n \times \binom{m-1+d}{d}$ further unknowns in its polynomial part p. The given reconstruction problem (1), however, contains only N conditions. In order to eliminate the Q degrees of freedom, we require that the dual functional τ in the major part of s in (3) lies in the linear space

$$\mathcal{L}_m^\perp = \left\{\tau : \tau(p) = 0, \text{ for all } p \in \mathcal{P}_m^{d,n}\right\}$$

of all dual functionals whose action on any polynomial from $\mathcal{P}_m^{d,n}$ is zero.

Now solving the reconstruction problem (1) under linear constraints (5) with assuming (3) for the form of the interpolant s, amounts to solving the $(N \times Q)$-by-$(N \times Q)$ linear equation system

$$\begin{aligned} Ac + Pd &= u\big|_\Lambda && (4)\\ c^T P &= 0 && (5) \end{aligned}$$

where

$$A = (\lambda(\mu * \mathbf{\Phi}))_{\mu,\lambda\in\Lambda} \in \mathbb{R}^{N\times N} \quad \text{and} \quad P = (\lambda(p_\ell))_{\substack{\lambda\in\Lambda \\ 1\le\ell\le Q}} \in \mathbb{R}^{N\times Q}, \qquad (6)$$

with $p_1, \ldots, p_Q$ being a basis of $\mathcal{P}_m^{d,n}$.

By using a standard argument from radial basis function interpolation [24], it is straightforward to show that the linear system (4),(5) is well-posed, provided that $\mathbf{\Phi}$ is *conditionally positive definite*.

Definition 1 *We say that* $\mathbf{\Phi}$ *is* `conditionally positive definite` *of order* m, $\mathbf{\Phi} \in \mathbf{CPD}(m)$, *iff the quadratic form*

$$\sum_{\mu,\lambda\in\Lambda} c_\mu c_\lambda \lambda(\mu * \mathbf{\Phi})$$

is positive for any set Λ *of linearly independent functionals and any non-zero vector* $c = (c_\mu) \in \mathbb{R}^N \setminus \{0\}$ *satisfying* $c^T P = 0$, *i.e.*,

$$\sum_{\lambda\in\Lambda} \lambda(p) = 0, \qquad \text{for all } p \in \mathcal{P}_m^{d,n}. \qquad (7)$$

We say that $\mathbf{\Phi}$ *is* `positive definite`, $\mathbf{\Phi} \in \mathbf{PD}$, *iff* $\mathbf{\Phi}$ *is conditionally positive definite of order* 0.

In order to keep this paper widely self-contained, we repeat that quite instructive standard argument.

Theorem 1 *Suppose* $\mathbf{\Phi} \in \mathbf{CPD}(m)$. *Then the linear reconstruction problem (1) has under constraints (7) a unique solution* s *of the form (3), provided that for* $p \in \mathcal{P}_m^{d,n}$, *the implication*

$$\lambda(p) = 0, \quad \textit{for all } \lambda \in \Lambda \qquad \Longrightarrow \qquad p = 0, \tag{8}$$

holds.

Proof: First note that the problem (1),(7) is equivalent to the problem (4),(5). In order to show that the linear system (4),(5) has a unique solution for $\mathbf{\Phi} \in \mathbf{CPD}(m)$, we regard the homogeneous system belonging to (4),(5). Multiplying (4) from left with c^T with using (5) immediately yields $c^T A c = 0$. But since $\mathbf{\Phi} \in \mathbf{CPD}(m)$, this implies $c = 0$, and so (4) becomes $Pd = 0$. In order to see that also $d = 0$, note that (8) is equivalent to requiring P is injective. Hence, the solution of the homogeneous system belonging to (4),(5) is uniquely given by zero, which completes our proof. ■

Note that the condition (8), often referred to as the *unisolvence* of Λ with respect to the polynomials $\mathcal{P}_m^{d,n}$, is equivalent to requiring that each polynomial $p \in \mathcal{P}_m^{d,n}$ can uniquely be reconstructed from its samples $\{\lambda(p) : \lambda \in \Lambda\}$. This condition is rather weak. Indeed, for the special case, where $m = 0$, the condition (8) is empty, and so the interpolant s in (3) contains no polynomial part. In this case, according to Theorem 1, it it sufficient to require $\mathbf{\Phi} \in \mathbf{PD}$ in order to guarantee the well-posedness of reconstruction problem (1). Let us formulate this important observation in a seperate corollary.

Corollary 1 *For* $\mathbf{\Phi} \in \mathbf{PD}$, *the reconstruction problem (1) has a unique solution* s *of the form*

$$s(x) = \sum_{\mu \in \Lambda} c_\mu (\mu * \mathbf{\Phi}),$$

where the unknown coefficients $c = (c_\mu)_{\mu \in \Lambda}$ *of* s *can be computed by solving the linear equation system* $Ac = u\big|_\Lambda$, *whose coefficient matrix* A *in (6) is positive definite.* ■

In the remainder of this section, we show that a *diagonal* $\mathbf{\Phi}$ is conditionally positive definite of order m, if and only if all its diagonal components ϕ_{jj}, $1 \leq j \leq n$, are conditionally positive definite of order m.

To this end, first note that the Definition 1 for $\mathbf{CPD}(m)$ covers the special case where $n = 1$, so that it makes sense to require $\phi_{jj} \in \mathbf{CPD}(m)$ for the individual scalar-valued components in the diagonal of $\mathbf{\Phi}$. But for this special case, the class of conditionally positive definite functions is well-understood [24], see also the characterization of the function class $\mathbf{CPD}(m)$ in [25, 26, 27].

Now it is straightforward to show that the following observation is true.

Lemma 1 *Let $\mathbf{\Phi} : \mathbb{R}^d \to \mathbb{R}^{n \times n}$ be a diagonal matrix-valued function of the form*

$$\mathbf{\Phi} = \begin{bmatrix} \phi_{11} & & \\ & \ddots & \\ & & \phi_{nn} \end{bmatrix},$$

with scalar-valued diagonal components ϕ_{jj}, $1 \leq j \leq n$. Then, $\mathbf{\Phi}$ is conditionally positive definite of order m, iff every diagonal component ϕ_{jj} is conditionally positive definite of order m, i.e.,

$$\phi_{jj} \in \mathbf{CPD}(m) \quad \textit{for all } 1 \leq j \leq n \qquad \Longleftrightarrow \qquad \mathbf{\Phi} \in \mathbf{CPD}(m).$$

Proof: Regard for any pair $\mu, \lambda \in \Lambda$ the quadratic form

$$\begin{aligned} \sum_{\mu,\lambda \in \Lambda} c_\mu c_\lambda \mu(\lambda * \mathbf{\Phi}) &= \sum_{\mu,\lambda \in \Lambda} c_\mu c_\lambda \sum_{j,k=1}^{n} \mu_j^{\mathbf{x}}(\lambda_k^{\mathbf{y}} \phi_{jk}(\mathbf{x}-\mathbf{y})) \qquad (9) \\ &= \sum_{\mu,\lambda \in \Lambda} c_\mu c_\lambda \sum_{j=1}^{n} \mu_j^{\mathbf{x}}(\lambda_j^{\mathbf{y}} \phi_{jj}(\mathbf{x}-\mathbf{y})) \\ &= \sum_{j=1}^{n} \left[\sum_{\mu,\lambda \in \Lambda} c_\mu c_\lambda \mu_j^{\mathbf{x}}(\lambda_j^{\mathbf{y}} \phi_{jj}(\mathbf{x}-\mathbf{y})) \right]. \qquad (10) \end{aligned}$$

Now, according to [25], for each $\phi_{jj} \in \mathbf{CPD}(m)$ the quadratic form

$$\sum_{\mu,\lambda \in \Lambda} c_\mu c_\lambda \mu_j^{\mathbf{x}}(\lambda_j^{\mathbf{y}} \phi_{jj}(\mathbf{x}-\mathbf{y})) = \sum_{\mu,\lambda \in \Lambda} c_\mu c_\lambda \mu_j(\lambda_j * \phi_{jj})$$

is positive for any non-vanishing $c = (c_\lambda)_{\lambda \in \Lambda} \in \mathbb{R}^N \setminus \{0\}$, satisfying

$$\sum_{\lambda \in \Lambda} c_\lambda \lambda_j(p) = 0, \qquad \text{for all } p \in \mathcal{P}_m^{d,1}.$$

But this, in combination with the representation (10) for the quadratic form (9), immediately implies that (9) is positive for all non-vanishing $c \in \mathbb{R}^N \setminus \{0\}$ satisfying

$$\sum_{\lambda \in \Lambda} c_\lambda \lambda(p) = 0, \qquad \text{for all } p \in \mathcal{P}_m^{d,n},$$

and so $\mathbf{\Phi}$ is conditionally positive definite of order m, $\mathbf{\Phi} \in \mathbf{CPD}(m)$.

As for the converse, it is easy to see from (10) that $\mathbf{\Phi} \in \mathbf{CPD}(m)$ implies $\phi_{jj} \in \mathbf{CPD}(m)$, for any $1 \leq j \leq n$, which completes our proof. ■

3 Local Vector Field Reconstruction in Two Dimensions

We now formulate the specific vector reconstruction problem that we wish to address in hydrodynamical applications, some of which are discussed in Section 5. In this particular case we work with planar vector fields $\mathbf{u} : \mathbb{R}^2 \to \mathbb{R}^2$, $\mathbf{u} = [u_1, u_2]$, so that $d = 2$ and $n = 2$. Moreover, we assume we are given a (possibly scattered) set $\mathbf{X} = \{\mathbf{x}_1, \ldots, \mathbf{x}_N\} \subset \mathbb{R}^2$ of N pairwise distinct planar points, where each point $\mathbf{x}_i \in \mathbf{X}$ corresponds to a unit vector $\mathbf{n}_i = [n_i^1, n_i^2]^T \in \mathbb{R}^2$, $1 \leq i \leq N$.

Now we wish to reconstruct a smooth vector field $\mathbf{u} : \mathbb{R}^2 \to \mathbb{R}^2$, from given scalar samples $u_i = \mathbf{u}(\mathbf{x}_i) \cdot \mathbf{n}_i \in \mathbb{R}$, for $1 \leq i \leq N$. According to the more general reconstruction problem, formulated in the previous section, we are concerned with solving the reconstruction problem

$$\lambda_i(\mathbf{u}) = \lambda_i(\mathbf{s}), \qquad \text{for } 1 \leq i \leq N,$$

where $\lambda_i = \delta_{\mathbf{x}_i} \cdot \mathbf{n}_i$, and where $\delta_{\mathbf{x}_i}$ denotes the Dirac point evaluation functional, defined as $\delta_{\mathbf{x}_i}(\mathbf{u}) = \mathbf{u}(\mathbf{x}_i)$, for $1 \leq i \leq N$.

Now the recovery function $\mathbf{s} : \mathbb{R}^2 \to \mathbb{R}^2$ is required to have the form (3). Hence, each term in the major part of $\mathbf{s}$ has the form

$$(\mu * \mathbf{\Phi})(\mathbf{x}) = \mathbf{\Phi}(\mathbf{x} - \mathbf{x}_i) \cdot \mathbf{n} = \begin{bmatrix} \phi_{11}(\mathbf{x} - \mathbf{x}_i) n_i^1 \\ \phi_{22}(\mathbf{x} - \mathbf{x}_i) n_i^2 \end{bmatrix}. \tag{11}$$

In the implementation of RBF reconstruction in Sections 4 and 5, we prefer to work with positive definite radial basis functions, i.e., $\mathbf{\Phi} \in \mathbf{PD}$. Recall from Lemma 1 that in this case we require $\phi_{11}, \phi_{22} \in \mathbf{PD}$. Possible choices for the diagonal entries in $\mathbf{\Phi}$ are, for instance, the Gaussians $\phi(r) = e^{-\alpha r^2} \in \mathbf{PD}$ for any $\alpha > 0$, or the inverse multiquadrics, $\phi(r) = (c^2 + r^2)^{-1/2} \in \mathbf{PD}$ for $c \neq 0$. In this case, no polynomial part is included in the scheme, in which case the interpolant s has the form

$$s(\mathbf{x}) = \sum_{i=1}^{N} c_i \begin{bmatrix} \phi_{11}(\mathbf{x} - \mathbf{x}_i) n_i^1 \\ \phi_{22}(\mathbf{x} - \mathbf{x}_i) n_i^2 \end{bmatrix},$$

whose unknown coefficients $c = (c_1, \ldots, c_N)^T \in \mathbb{R}^N$ are computed by solving the linear system $Ac = u\big|_\Lambda$ in (4).

4 Comparison between RBF and RT Vector Field Reconstruction

In this section, we report on selected numerical experiments in order to discuss the *effective* accuracy order of RBF reconstruction by using the positive definite

Gaussians, i.e., where we let $\phi_{11}(r) \equiv \phi_{22}(r) \equiv \phi(r) = e^{-r^2/4} \in \mathbf{PD}$. Due to the theory of RBF interpolation [3, Chapter 11], spectral convergence rates are expected in this case. One should note, however, that the spectral condition number $\kappa(A)$ of the arising interpolation matrix A is, as a function of the minimal distance between different sample points, of exponential growth. This is due to the uncertainty principle of RBF reconstruction, which says that none of the commonly used radial basis functions manages to combine good approximation behaviour with a numerically stable reconstruction process. This dilemma, discovered by Schaback [28], requires carefully selecting available method parameters in order to obtain a reasonable trade-off between the two conflicting requirements, i.e., high approximation order and good numerical stability.

Our numerical results concerning RBF interpolation, as reflected by Tables 1 and 2, are involving four different stencils of sizes $N = 3, 9, 15, 21$. The four stencils are shown in Figure 1. Note that for either stencil, the interpolation points are lying on a hexagonal grid. This is in order to reasonably balance the methods' resulting accuracy, on the one hand, and their numerical stability, on the other hand. For further motivation concerning this particular point sampling we refer to our previous findings in [2, Subsection 3.9].

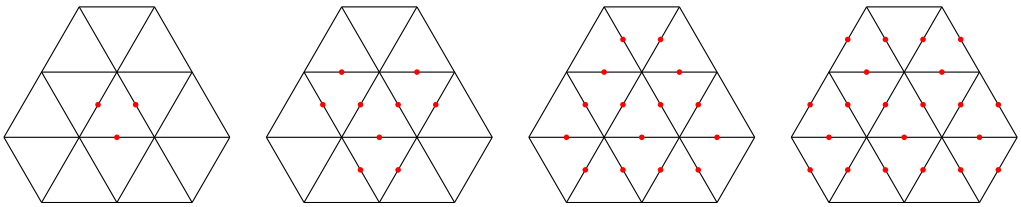

(a) $N = 3$ **(b)** $N = 9$ **(c)** $N = 15$ **(d)** $N = 21$

Figure 1: Stencils of different sizes N for accuracy tests.

To evaluate the methods' approximation behaviour, we consider the resulting maximal error $\epsilon = \|s-u\|_\infty$ among the barycenters of the triangles in the stencils' corresponding Delaunay triangulation, see Figure 1. Similar to the assessment in our previous paper [14] for RBF reconstruction for the scalar case, we consider using the vector field

$$\begin{pmatrix} u \\ v \end{pmatrix} = \begin{pmatrix} \cos(k\,\pi\,(x-\frac{1}{4}))\sin(k\,\pi\,(y-\frac{1}{4})) \\ \sin(k\,\pi\,(x-\frac{1}{4}))\cos(k\,\pi\,(y-\frac{1}{4})) \end{pmatrix},$$

where increasingly denser data sets are used. The data sets were generated by scaling the interpolation points $\mathbf{X}$, so that $q_{\mathbf{X}} \equiv h = 2^{-i}$, $i = 0, 1, 2, 3, 4$, for the *separation distance*

$$q_{\mathbf{X}} = \min_{\substack{\mathbf{x},\mathbf{y} \in \mathbf{X} \\ \mathbf{x} \neq \mathbf{y}}} \|\mathbf{x} - \mathbf{y}\|$$

of the interpolation points in stencil $\mathbf{X}$.

The numerical results in Table 1 show the approximation error $\epsilon(\mathrm{RT}_0)$ obtained when using Raviart-Thomas elements of order zero, RT_0, in comparision with the approximation error $\epsilon(\mathrm{RBF})$ from RBF reconstruction by Gaussians. Table 1 also shows the corresponding spectral condition number $\kappa(A)$ of the RBF interpolation matrix A. Moreover, estimates for convergence rates, obtained by the two different methods, RBF and RT_0, are displayed in Table 1. The test were performed for a decreasing sequence of separation distances $h = 2^{-i}$, $i = 0, 1, 2, 3, 4$, just before the linear system of RBF interpolation becomes numerically unstable, due to too large spectral condition numbers, cf. the last column of Table 1.

Table 1: Comparison between RT_0 and RBF reconstruction by Gaussians for the 15-point stencil in Figure 1 **(c)**. The relative approximation error ϵ, approximate convergence rate, and spectral condition number $\kappa(A)$ of the corresponding RBF interpolation matrix A are shown, respectively.

h	$\epsilon(\mathrm{RT}_0)$	rate	$\epsilon(\mathrm{RBF})$	rate	$\kappa(A)$
2^{-0}	$7.177 \cdot 10^{-1}$	-	$7.248 \cdot 10^{-1}$	-	$3.625 \cdot 10^{4}$
2^{-1}	$3.070 \cdot 10^{-1}$	1.225	$1.151 \cdot 10^{-1}$	2.654	$2.511 \cdot 10^{6}$
2^{-2}	$1.349 \cdot 10^{-1}$	1.187	$1.451 \cdot 10^{-2}$	2.988	$1.650 \cdot 10^{8}$
2^{-3}	$6.238 \cdot 10^{-2}$	1.112	$1.773 \cdot 10^{-3}$	3.033	$1.064 \cdot 10^{10}$
2^{-4}	$2.991 \cdot 10^{-2}$	1.060	$2.178 \cdot 10^{-4}$	3.025	$6.833 \cdot 10^{11}$

All linear systems were solved by Gauss elimination, and for the results in Table 1, the 15-point stencil of Figure 1 **(c)** was utilized. As expected, we obtain linear convergence for Raviart-Thomas reconstruction of order zero, whereas RBF reconstruction yields third order accuracy, see Table 1. Moreover, despite the small separation distance of up to $h = 2^{-4}$, RBF interpolation is still very robust. But for smaller values of h, the corresponding linear system is ill-conditioned, so that it does not make sense to further evaluate the method's accuracy.

In a second test case, we compare the approximation quality of Gaussian RBF reconstruction for four different stencils of sizes $N = 3, 9, 15, 21$, displayed in Figure 1. Our numerical results are reflected by Table 2 (for $N = 3, 9, 21$) and Table 1 (for $N = 15$).

Not too surprisingly, the accuracy order is increasing with the size N of the utilized stencils, see Table 1 and 2. Indeed, the stencil with $N = 21$ interpolation points yields the best accuracy rate among the four stencils, namely slightly

Table 2: RBF reconstruction by Gaussians for stencils of different sizes N, see Figure 1.

h	ϵ $(N=3)$	rate	ϵ $(N=9)$	rate	ϵ $(N=21)$	rate
2^{-0}	$7.177 \cdot 10^{-1}$	-	$7.156 \cdot 10^{-1}$	-	$7.180 \cdot 10^{-1}$	-
2^{-1}	$3.070 \cdot 10^{-1}$	1.225	$1.251 \cdot 10^{-1}$	2.516	$8.767 \cdot 10^{-2}$	3.034
2^{-2}	$1.349 \cdot 10^{-1}$	1.187	$1.769 \cdot 10^{-2}$	2.823	$1.181 \cdot 10^{-2}$	2.892
2^{-3}	$6.238 \cdot 10^{-2}$	1.112	$2.594 \cdot 10^{-3}$	2.770	$1.819 \cdot 10^{-3}$	2.698
2^{-4}	$2.991 \cdot 10^{-2}$	1.060	$4.270 \cdot 10^{-4}$	2.603	$9.958 \cdot 10^{-5}$	4.192

above order four, whereas the stencil with $N = 3$ points yields first order accuracy only, which is about comparable to the convergence rate obtained from Raviart-Thomas reconstruction of order zero, RT_0. In other words, for any stencil with more than three interpolation points, RBF reconstruction by Gaussians is superior to RT_0 reconstruction. Further supporting numerical results were recently recorded in [29].

5 Application to Fluid Dynamics Problems

In this section, we discuss applications of the proposed RBF reconstruction method to computational fluid dynamics models. More specifically, we will refer to models for the shallow water equations using discretization approaches in which the velocity field is represented by its normal components with respect to the mesh edges. The shallow water equations model the two dimensional flow of a thin fluid layer in domains whose characteristic wave length in the horizontal is much larger than the fluid depth. The shallow water equations result from the Navier-Stokes equations when the hydrostatic assumption holds and only barotropic and adiabatic motions are considered. Furthermore, a vertical average is performed, so that only mean values for the velocities in the horizontal directions are considered, see e.g. [30]. The shallow water equations can be written as

$$\frac{\partial h}{\partial t} + \nabla \cdot \Big(H\mathbf{v} \Big) = 0, \tag{12}$$

$$\frac{\partial \mathbf{v}}{\partial t} + (\mathbf{v} \cdot \nabla)\mathbf{v} = -f\mathbf{k} \times \mathbf{v} - g\nabla h. \tag{13}$$

Here, $\mathbf{v}$ denotes the two-dimensional velocity vector, $\mathbf{k}$ is the radial unit vector perpendicular to the plane on which $\mathbf{v}$ is defined (or to the local tangent plane, in case of applications in spherical geometry), h is the height of the fluid layer above a reference level, $H = h - h_s$ is the thickness of the fluid layer, h_s is the orographic or bathymetric profile, g is the gravitational constant, and f

is the Coriolis parameter. This formulation is the starting point for Eulerian-Lagrangian discretizations. Another widely used formulation for applications to large scale atmospheric dynamics is the so called *vector invariant form*, see e.g. [31], which can be written as

$$\frac{\partial \mathbf{v}}{\partial t} = -(\zeta + f)\mathbf{k} \times \mathbf{v} - \nabla\Big(gh + K\Big). \tag{14}$$

Here, ζ is the component of relative vorticity in the direction of $\mathbf{k}$ and K denotes the kinetic energy. This formulation is usually the starting point for the derivation of energy, potential enstrophy and potential vorticity preserving discretizations, see e.g. [32].

Spatial discretizations with staggered arrangements of the discrete variables are popular for the shallow water equations, since they allow for better representation of the gravity wave propagation, see e.g. [33]. On unstructured grid, an analog of a staggered discretization is given by the zero order Raviart-Thomas elements RT_0, see e.g. [17]. Although high order RT elements are also available, the low order ones, RT_0 elements, lead more easily to numerical methods that exhibit important discrete conservation properties, such as discrete mass or vorticity preservation. These properties are important for a number of applications and various methods which take advantage of them is discussed in the two following subsections. The main point here is that the accuracy of these models has been limited so far by the first order convergence of the RT_0 elements. As it will be shown in the following, matrix-valued RBF reconstruction can effectively improve these methods, by achieving a more accurate discretization of the nonlinear momentum advection terms, either in Eulerian or in semi-Lagrangian formulations. Although in general this is not sufficient to raise the convergence order of the overall methods, models employing RBF reconstructions display significantly smaller errors and have in general less numerical dissipation, making their use attractive for a number of applications.

5.1 Eulerian Shallow Water Models

Eulerian discretizations of equations (12),(14) have been proposed in [20, 21], which preserve discrete approximations of mass, vorticity and potential enstrophy. These properties are important for numerical models of general atmospheric circulation, especially for applications to climate modelling. The two time level, semi-implicit scheme in these papers used RT reconstruction to compute the nonlinear terms in the discretization of (14). Here, we will compare results obtained with a three-time level, semi-implicit time discretization, coupled to the potential enstrophy preserving spatial discretization of [21], using either the Raviart-Thomas algorithm or a vector RBF reconstruction of the velocity field necessary for the solution of equation (14). For these tests, we employed RBF reconstruction using the positive definite Gaussians, where $\phi(r) = e^{-r^2}$. Moreover, a 9-point stencil was employed, see Figure 1 **(b)**, using the normal components

to the edges of the triangle on which the interpolation is being carried out and to the edges of its nearest neighbours (i.e., of the triangles which have common edges with it).

We consider one stationary and two non-stationary test cases for the shallow water equations belonging to the set of standard benchmark problems introduced in [31]. First, we study how the algorithm performs when applied to test case 3 of the standard shallow water suite [31], which consists of a steady-state, zonal geostrophic flow with a narrow jet at midlatitudes. For this test case, an analytic solution is available, so that errors can be computed by applying the numerical method at different resolutions. The values of the relative error in various norms, as computed at day 2 with different spatial resolutions and with time step $\Delta t = 1800$ s, is displayed in Tables 3 and 4 for both Raviart Thomas elements and vector RBF reconstruction, respectively. It can be observed that, although the convergence rates remain approximately unchanged (due to the fact that the approximately second order discretization of the geopotential gradient was the same in both tests), the errors both in the height and velocity fields have decreased by an amount that ranges approximately between 30 % and 50 %.

Table 3: Relative errors for nonlinear terms in shallow water test case 3 obtained by using RT_0 reconstruction.

Level	ℓ_2-error, h	ℓ_2-error, $\mathbf{v}$	ℓ_∞-error, h	ℓ_∞-error, $\mathbf{v}$
3	7.42e-3	0.25	2.53e-2	0.33
4	1.94e-3	5.9e-2	8.1e-3	9.1e-2
5	6.05e-4	1.27e-2	2.9e-3	1.87e-2
6	2.54e-4	3.19e-3	1.24e-3	4.17e-3

Table 4: Relative errors for nonlinear terms in shallow water test case 3 obtained by using Gaussian RBF reconstruction on a 9-point stencil, see Figure 1 **(b)**.

Level	ℓ_2-error, h	ℓ_2-error, $\mathbf{v}$	ℓ_∞-error, h	ℓ_∞-error, $\mathbf{v}$
3	7.27e-3	0.16	2.08e-2	0.17
4	1.52e-3	3.38e-2	6.74e-3	5.77e-2
5	4.05e-4	7.7e-3	1.7e-3	1.22e-2
6	1.45e-4	2.11e-3	4.8e-4	2.89e-3

We have then considered the non-stationary test case 5 of [31], for which the initial datum consists of a zonal flow impinging on an isolated mountain of conical shape. The imbalance in the initial datum leads to the development of a wave which propagates all around the globe. This test is relevant to understand the response of the numerical model to orographic forcing and it has been a common benchmark since the development of the first spectral models. Plots of

the meridional velocity component at simulation day 5 are shown in Figure 2, as computed using the constant timestep $\Delta t = 900$ s on an icosahedral grid at spatial resolution of approximately 240 km. We observe that the meridional velocity field obtained by using RT_0 finite elements is much less regular than that obtained by RBF reconstruction, which complies with previous results obtained in similar reference simulations at higher resolution.

Finally, we have considered the non-stationary test case 6 of [31], for which the initial datum consists of a Rossby-Haurwitz wave of wavenumber 4. This type of wave is an analytic solution for the barotropic vorticity equation, which can also be used to test shallow water models on a time scale of up to 10-15 days. The relative vorticity field is shown in Figure 3, as computed at day 5 with a timestep of $\Delta t = 900$ s on an icosahedral grid with a spatial resolution of approximately 240 km. It can be observed that, when using RT_0 reconstruction, the structure of some vorticity extrema is disrupted, while spurious maxima and minima appear close to the poles. This is in contrast to the more regular field obtained by RBF reconstruction, which better complies with high resolution reference simulations. Furthermore, the relative change in total energy for both model runs is displayed in Figure 3. It can be observed that total energy loss is reduced by approximately 30 % when using RBF reconstruction, thus improving the energy conservation properties of the model, which conserves potential enstrophy but not energy as discussed in [21]. We remark that for Eulerian models, additional computational costs required for RBF reconstruction can significantly be reduced. Indeed, it is possible to compute for each grid cell a set of time independent coefficients which yield the velocity vector at the cell center as linear combination of the velocity components at the points included in the RBF stencil. For the model runs described above, it was observed that RBF reconstruction increases, in comparison with the simpler scheme RT_0, the required CPU time by approximately 20 %.

5.2 Eulerian-Lagrangian Shallow Water Models

Numerical methods for the shallow water equations using formulation (12),(13) have been proposed in [22, 23], which couple a mass conservative, semi-implicit discretization on unstructured Delaunay meshes to an Eulerian-Lagrangian treatment of momentum advection. The resulting methods are highly efficient due to their rather weak stability restrictions, while mass conservation allows for their practical (and successful) application to a number of pollutant and sediment transport problems. A key step of the Eulerian-Lagrangian method is the interpolation at the foot of characteristic lines, which in the papers quoted above is performed by RT_0 elements or by low order interpolation procedures based on area weighted averaging. These interpolators have at most first order convergence rate and can introduce large amounts of numerical diffusion, which limits their applicability especially in long term simulations.

Firstly, the test proposed in [12] has been carried out, in which a 800 m long

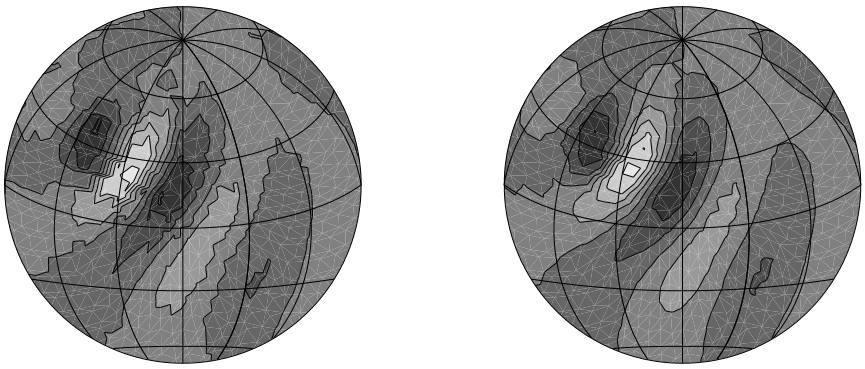

(a) Reconstruction by RT_0 **(b)** Reconstruction by Gaussian RBF

Figure 2: Meridional velocity in shallow water test case 5, obtained by **(a)** RT_0 reconstruction **(b)** Gaussian RBF reconstruction on a 9-point stencil. The contour line spacing is 6 ms^{-1}.

and 800 m wide basin was considered. The domain was discretized by an unstructured triangular mesh with 26,812 elements and 13,868 nodes, corresponding to a horizontal resolution of approximately 2 km. The basin depth was taken to be 20 m. A periodic inflow boundary condition was imposed on the free surface, with an amplitude of 1 m and a period of approximately 12 h. The resulting wavefront, computed after approximately 30 h by the Eulerian-Lagrangian method of [23], with using either RT_0 elements or RBF reconstruction at the foot of the characteristic, is displayed in Figure 5, It can be observed that for RBF reconstruction the wavefront is much sharper and the computed discharge rate at a given location along the basin reaches considerably higher values. The maximum in the free surface elevation (which would be equal to the maximum boundary value in the linear regime) is better captured by approximately 10 %. We remark that for specific quantities, such as free surface elevation, this leads to significant improvements in a number of relevant applications, such as flooding prediction in the Venice Lagoon, which is at end of a closed sea basin of approximately the same magnitude.

Furthermore, another shallow water test involving a closed rectangular basin, 150 m long and 15 m wide, was performed, whose discretization is given by an unstructured triangular mesh with 3,646 elements and 1,984 nodes. For the free surface, an unbalanced initial datum was assumed, given by $\eta(x) = h_0 \cos(x\pi/150)$. The amplitude of the disturbance was taken to be equal to $h_0 = 0.1$ and the initial velocity fields were assumed to be zero. The resulting free oscillations have been simulated by the same method described above, using again either RT_0 elements or matrix-valued RBFs for reconstruction at the foot of the characteristic. The free oscillations of the fluid were simulated for a total

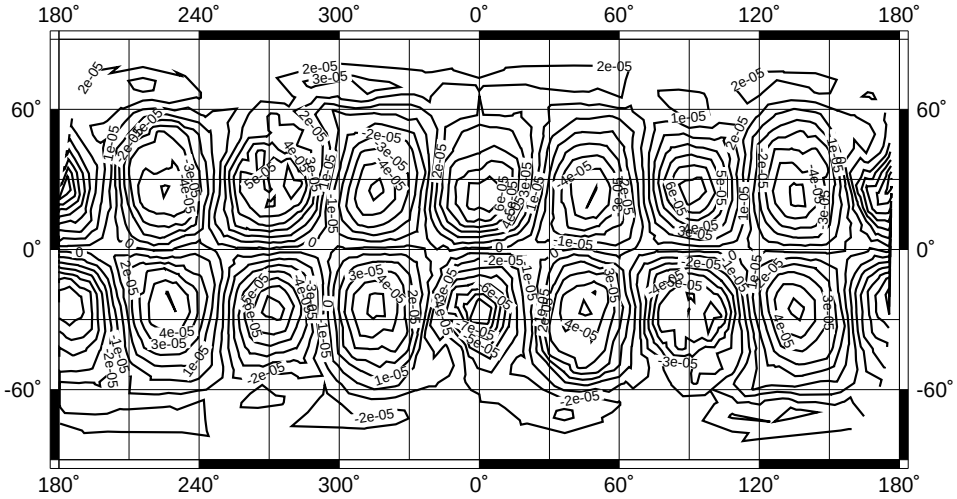

(a) Reconstruction by RT_0

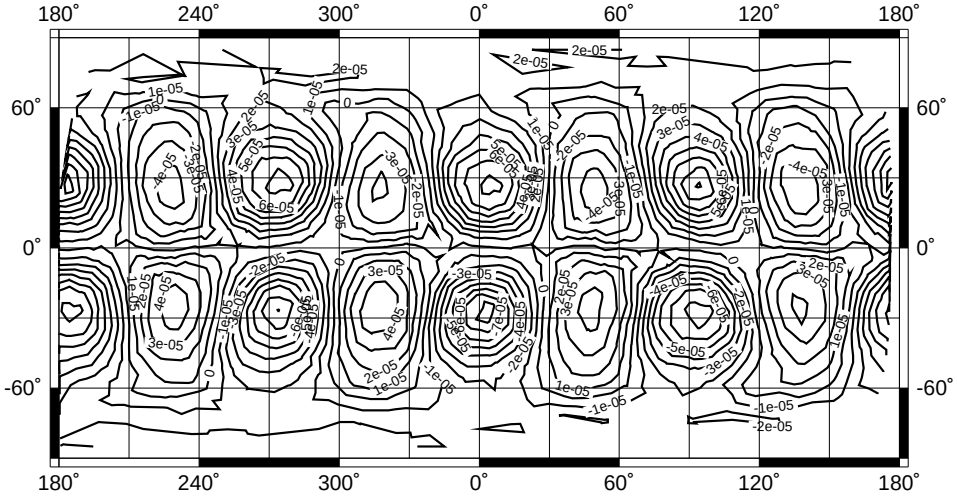

(b) Reconstruction by Gaussian RBF

Figure 3: Relative vorticity in shallow water test case 6, obtained by **(a)** RT_0 reconstruction **(b)** Gaussian RBF reconstruction on a 9-point stencil. The contour line spacing is 10^{-5} ms^{-1}.

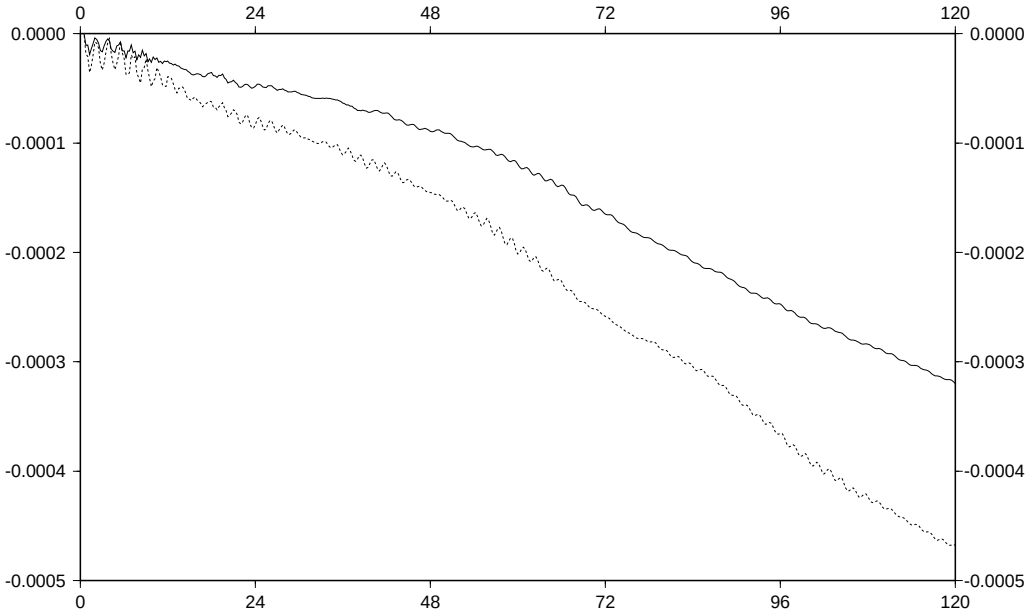

Figure 4: Relative decay in total energy in shallow water test case 6, obtained by RT_0 reconstruction (dotted line) and by Gaussian RBF reconstruction on a 9-point stencil (solid line).

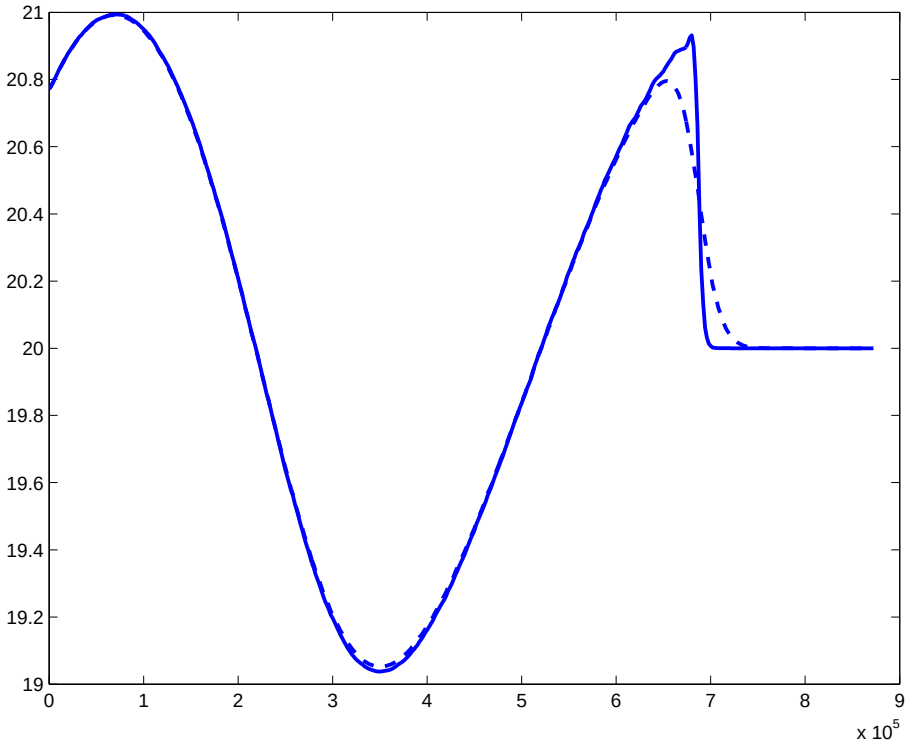

Figure 5: Free surface elevation in long channel test, obtained from RT_0 reconstruction (dotted line) and Gaussian RBF reconstruction on a 9-point stencil (solid line).

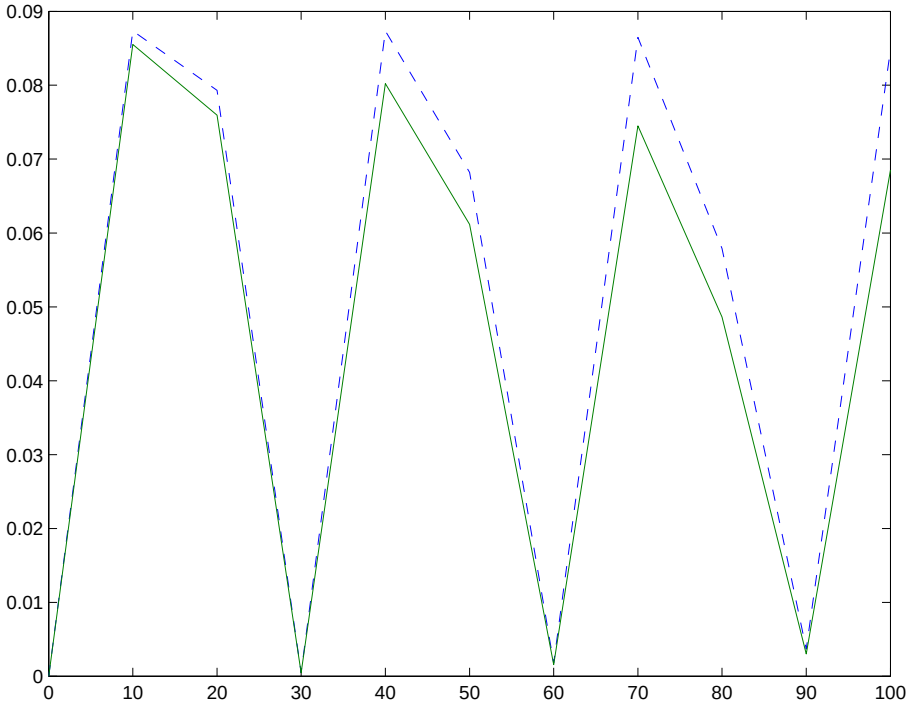

Figure 6: Kinetic energy for free oscillations test with Eulerian-Lagrangian model, obtained by RT_0 reconstruction (solid line) and Gaussian RBF reconstruction on a 9-point stencil (dotted line).

of 100 s at time step $\Delta t = 0.1$ s. The time evolution of kinetic energy is shown in Figure 6, while the height field values computed throughout the simulation in an element close to one of the boundaries are shown in Figure 7. It can be observed that the energy dissipation caused by the interpolation of the Eulerian-Lagrangian method is reduced by 20 % when using RBF reconstruction, whereas the maxima and minima in the height field are improved by approximately 10 %.

In other tests, even larger improvements were observed. For example, a square domain of width 20 m was considered, which was discretized by an unstructured triangular mesh with 3,984 elements and 2,073 nodes. A constant basin depth of 2 m was assumed. At initial time, still water was assumed and the free surface profile was taken to be a Gaussian hill centered at the center of the domain, with amplitude 0.1 m and standard deviation 2 m. In absence of any explicit dissipative term, the total energy of the system should be conserved. The free oscillations of the fluid were simulated for a total of 6 s at a constant time step $\Delta t = 0.01$ s. The time evolution of total energy is shown in Figure 8. It can be observed that the energy dissipation caused by the interpolation of the Eulerian-Lagrangian method is reduced by 40 % when using RBF reconstruction.

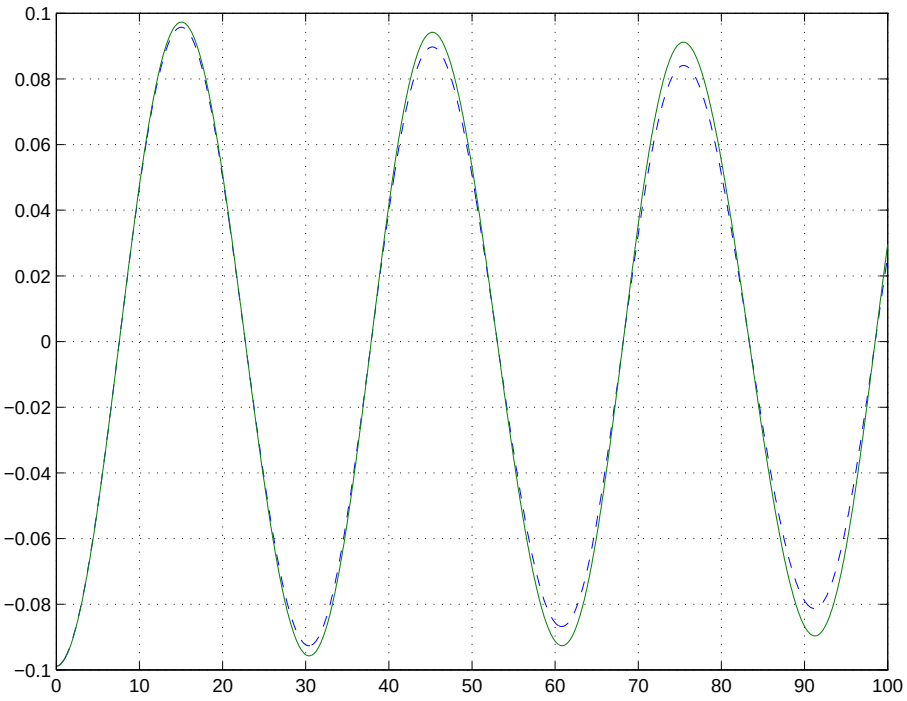

Figure 7: Height field time series at boundary element for free oscillations test with Eulerian-Lagrangian model, obtained by RT_0 reconstruction (solid line) and Gaussian RBF reconstruction on a 9-point stencil (dotted line).

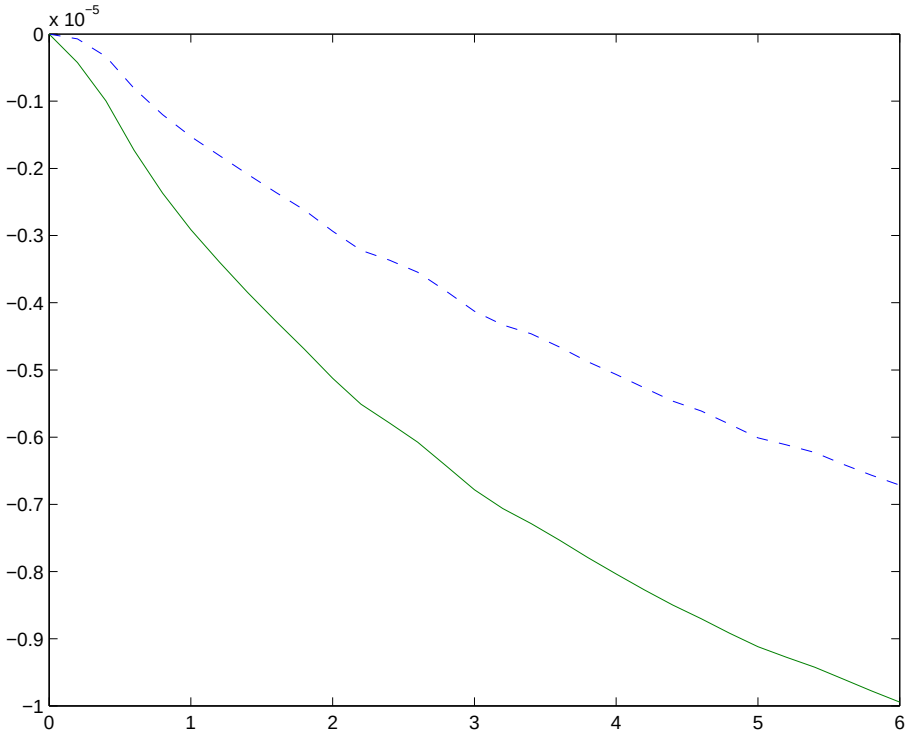

Figure 8: Relative change in total energy for free oscillations test with Eulerian-Lagrangian model, obtained by RT_0 reconstruction (solid line) and Gaussian RBF reconstruction on a 9-point stencil (dotted line).

We remark that in the case of Eulerian-Lagrangian models the extra computational cost due to the use of RBF reconstruction is higher than in the Eulerian case. This is because the coefficients which yield the velocity vector at the cell center as linear combination of the velocity components have to be recomputed at each time step for each of the trajectory departure points.

6 Conclusion

The utility of matrix-valued radial basis functions for accurate reconstruction of vector fields in fluid dynamics problems has been demonstrated. The theory of RBF reconstruction has been reviewed and adapted to applications in computational fluid dynamics. Important computational aspects concerning the implementation of the RBF reconstruction method were discussed. A number of supporting numerical tests have shown that RBF reconstruction improves the accuracy of low order Raviart-Thomas (RT) elements, RT_0, while retaining important discrete conservation properties, unlike high order RT elements.

Acknowledgements

The authors were partly supported by the Max-Planck Institute for Meteorology, Hamburg, through the ICON project. Many useful conversations with W. Sawyer on the application of RBFs in computational fluid dynamics are gratefully acknowledged, as well as contributions by T. Heinze and L. Kornblueh to the development of the ICON shallow water model.

References

[1] M. D. Buhmann, Radial Basis Functions, Cambridge University Press, Cambridge, UK, 2003.

[2] A. Iske, Multiresolution Methods in Scattered Data Modelling, Springer, Berlin, 2004.

[3] H. Wendland, Scattered Data Approximation, Cambridge University Press, Cambridge, UK, 2005.

[4] C. Franke, R. Schaback, Convergence order estimates of meshless collocation methods using radial basis functions, Adv. Comput. Math. 8 (1998) 381–399.

[5] C. Franke, R. Schaback, Solving partial differential equations by collocation using radial basis functions, Appl. Math. Comput. 93 (1998) 73–82.

[6] H. Wendland, Meshless Galerkin methods using radial basis functions, Math. Comp. 68 (1999) 1521–1531.

[7] J. Behrens, A. Iske, Grid-free adaptive semi-Lagrangian advection using radial basis functions, Comput. Appl. Math. 43 (2002) 319–327.

[8] J. Behrens, A. Iske, M. Käser, Adaptive meshfree method of backward characteristics for nonlinear transport equations, in: Meshfree Methods for Partial Differential Equations, Springer, Berlin, 2002, pp. 21–36.

[9] A. Iske, T. Sonar, On the structure of function spaces in optimal recovery of point functionals for ENO-schemes by radial basis functions, Numer. Math. 74 (1996) 177–202.

[10] T. Sonar, Optimal recovery using thin plate splines in finite volume methods for the numerical solution of hyperbolic conservation laws, IMA J. Numer. Anal. 16 (1996) 549–581.

[11] M. Käser, A. Iske, ADER schemes on adaptive triangular meshes for scalar conservation laws, J. Comput. Phys. 205 (2005) 486–508.

[12] S. M. Wong, Y. C. Hon, M. A. Golberg, Compactly supported radial basis functions for shallow water equations, Appl. Math. Comp. 127 (2002) 79–101.

[13] D. Y. L. Roux, C. A. Lin, A. Staniforth, An accurate interpolating scheme for semi-Lagrangian advection on an unstructured grid for ocean modelling, Tellus A 49A (1997) 119–138.

[14] G. Rosatti, L. Bonaventura, D. Cesari, Semi-implicit, semi-Lagrangian environmental modelling on Cartesian grids with cut cells, J. Comput. Phys. 204 (2005) 353–377.

[15] G. Rosatti, L. Bonaventura, R. Chemotti, High order interpolation methods for semi-Lagrangian models of mobile-bed river hydrodynamics on Cartesian grids with cut cells, Intern. J. Numer. Methods Fluids 47 (2005) 863–869.

[16] F. J. Narcowich, J. D. Ward, Generalized Hermite interpolation via matrix-valued conditionally positive definite functions, Math. Comp. 63 (1994) 661–687.

[17] A. Quarteroni, A. Valli, Numerical Approximation of Partial Differential Equations, Springer, Berlin-Heidelberg, 1994.

[18] P. A. Raviart, J. M. Thomas, A mixed finite element method for 2nd order elliptic problems, in: Mathematical aspects of finite element methods, Springer, 1977, pp. 292–315.

[19] F. Hermeline, Two coupled particle-finite volume methods using Delaunay-Voronoi meshes for the approximation of Vlasov-Poisson and Vlasov-Maxwell equations, J. Comput. Phys. 106 (1993) 1–18.

[20] L. Bonaventura, L. Kornblueh, T. Heinze, P. Ripodas, A semi-implicit method conserving mass and potential vorticity for the shallow water equations on the sphere, Intern. J. Numer. Methods Fluids 47 (2005) 863–869.

[21] L. Bonaventura, T. Ringler, Analysis of discrete shallow water models on geodesic Delaunay grids with C-type staggering, Monthly Weather Review 133 (2005) 2351–2373.

[22] V. Casulli, R. A. Walters, An unstructured grid, three-dimensional model based on the shallow water equations, Intern. J. Numer. Methods Fluids 32 (2000) 331–348.

[23] E. Miglio, A. Quarteroni, F. Saleri, Finite element approximation of quasi-3d shallow water equations, Computational Methods in Applied Mechanics and Engineering 174 (1999) 355–369.

[24] C. A. Micchelli, Interpolation of scattered data: distance matrices and conditionally positive definite functions, Constr. Approx. 2 (1986) 11–22.

[25] A. Iske, Reconstruction of functions from generalized Hermite-Birkhoff data, in: Approximation Theory VIII. Vol. 1: Approximation and Interpolation, World Scientific, Singapore, 1995, pp. 257–264.

[26] R. Schaback, H. Wendland, Characterization and construction of radial basis functions, in: Multivariate Approximation and Applications, Cambridge University Press, Cambridge, UK, 2001, pp. 1–24.

[27] Z. Wu, Hermite-Birkhoff interpolation of scattered data by radial basis functions, Approx. Theory Appl. 8 (2) (1992) 1–10.

[28] R. Schaback, Error estimates and condition numbers for radial basis function interpolation, Adv. Comput. Math. 3 (1995) 251–264.

[29] J. Baudisch, Accurate Reconstruction of Vector Fields Using Radial Basis Functions, Master's thesis, Munich University of Technology, Germany (2005).

[30] J. Pedlosky, Geophysical Fluid Dynamics, Springer, New York, 1987.

[31] D. L. Williamson, J. B. Drake, J. J. Hack, R. Jakob, P. N. Swarztrauber, A standard test set for numerical approximations to the shallow water equations in spherical geometry, J. Comput. Phys. 102 (1992) 211–224.

[32] A. Arakawa, V. Lamb, A potential enstrophy and energy conserving scheme for the shallow water equations, Monthly Weather Review 109 (1981) 18–136.

[33] D. A. Randall, Geostrophic adjustment and the finite-difference shallow water equations, Monthly Weather Review 122 (1994) 1371–1377.